Electron Bulk Acceleration and Thermalization at Earth's Quasiperpendicular Bow Shock

L.-J. Chen,[1,2,*] S. Wang,[1,2] L. B. Wilson III,[1] S. Schwartz,[3] N. Bessho,[1,2] T. Moore,[1] D. Gershman,[1] B. Giles,[1] D. Malaspina,[3] F. D. Wilder,[3] R. E. Ergun,[3] M. Hesse,[4] H. Lai,[5] C. Russell,[5] R. Strangeway,[5] R. B. Torbert,[6] A. F.-Vinas,[1] J. Burch,[6] S. Lee,[1] C. Pollock,[7] J. Dorelli,[1] W. Paterson,[1] N. Ahmadi,[3] K. Goodrich,[3] B. Lavraud,[8] O. Le Contel,[9] Yu. V. Khotyaintsev,[10] P.-A. Lindqvist,[11] S. Boardsen,[1,2] H. Wei,[5] A. Le,[12] and L. Avanov[1,2]

[1]*NASA, Goddard Space Flight Center, Greenbelt, Maryland 20771, USA*
[2]*Department of Astronomy, University of Maryland, College Park, Maryland 20747, USA*
[3]*Laboratory for Atmospheric and Space Physics, University of Colorado, Boulder, Colorado 80305, USA*
[4]*University of Bergen, Bergen 5020, Norway*
[5]*University of California, Los Angeles, Los Angeles, California 90095, USA*
[6]*Southwest Research Institute, San Antonio, Texas 78238, USA*
[7]*Denali Scientific, Healy, Alaska 99743, USA*
[8]*Institut de Recherche en Astrophysique et Planétologie, Université de Toulouse (UPS), CNRS, CNES, Toulouse, 31028 Cedex 4, France*
[9]*Laboratoire de Physique des Plasmas (UMR7648), CNRS/Ecole Polytechnique/Sorbonne Université/ Univ. Paris Sud/Observatoire de Paris, Paris, F91128 Palaiseau Cedex, France*
[10]*Swedish Institute of Space Physics, Uppsala SE-75121, Sweden*
[11]*KTH Royal Institute of Technology, Stockholm SE-11428, Sweden*
[12]*Los Alamos National Laboratory, Los Alamos, New Mexico 87545, USA*

(Received 25 January 2018; revised manuscript received 30 March 2018; published 31 May 2018)

Electron heating at Earth's quasiperpendicular bow shock has been surmised to be due to the combined effects of a quasistatic electric potential and scattering through wave-particle interaction. Here we report the observation of electron distribution functions indicating a new electron heating process occurring at the leading edge of the shock front. Incident solar wind electrons are accelerated parallel to the magnetic field toward downstream, reaching an electron-ion relative drift speed exceeding the electron thermal speed. The bulk acceleration is associated with an electric field pulse embedded in a whistler-mode wave. The high electron-ion relative drift is relaxed primarily through a nonlinear current-driven instability. The relaxed distributions contain a beam traveling toward the shock as a remnant of the accelerated electrons. Similar distribution functions prevail throughout the shock transition layer, suggesting that the observed acceleration and thermalization is essential to the cross-shock electron heating.

DOI: 10.1103/PhysRevLett.120.225101

Collisionless shocks are fundamentally nonlinear phenomena in which the plasma kinetic energy in the form of supersonic flows is dissipated into heat without the aid of binary collisions. The interaction between the solar wind and planetary magnetospheres and between the interstellar medium and supernova remnants gives rise to collisionless shocks that have stimulated intense research, e.g., Refs. [1–4]. Earth's bow shock is the most accessible laboratory for studying how the bulk flow energy is dissipated to heat ions and electrons. For strong shocks with a quasiperpendicular geometry (i.e., the angle between the upstream magnetic field and the shock normal is greater than 45°), while ion heating is commonly regarded as a result of particle reflection by electric and magnetic forces [5], the electron heating problem remains controversial [2].

The key controversy concerning electron heating lies in how and when irreversible dissipation occurs. A widely accepted picture of electron heating at the Earth's bow shock describes that the electron phase space is inflated by a quasistatic cross-shock potential accelerating (decelerating) incoming (escaping) electrons, conserving the first adiabatic invariant, and creates an inaccessible region at energies lower than the cross-shock potential energy of electrons [6–12]. The inaccessible region is postulated to be filled by wave-particle scattering, leading to thermalization and thus [8,12,13]. The picture is based on past observations of heated "flat-topped" distributions [6,13,14] and approximately isotropic temperature increase through the shock ramp [7,8,13]. However, the time resolution of previous electron measurements was not sufficient to resolve the acceleration and thermalization processes in the shock transition layer. Furthermore, the presence of intense, possibly transient, electron-scale electric field fluctuations [15–21] could invalidate the adiabatic

invariance assumption, thus calling into question the simple phase-space inflation picture [12]. The adiabatic invariant can also be broken by strong gradients in the electric field [18,22,23], leading to heating perpendicular to the magnetic field [24].

In this Letter, we present the observation of electron acceleration and thermalization in action using measurements from the Magnetospheric Multiscale (MMS) spacecraft [25]. The electron instrument onboard MMS is capable of obtaining a full 3D electron velocity distribution every 30 ms, a cadence 2 orders of magnitude higher than that achieved on previous missions and capable to resolve the acceleration and thermalization time scales for the event to be discussed.

Method.—The measurements come from the MMS four-spacecraft mission [25] when MMS crosses the bow shock at Earth. The location of MMS during the shock crossing at 2015-11-04/05:28:20-55 UT is [10.6, 2.5, −0.5] R_E in the geocentric solar ecliptic (GSE) coordinate, very close to the nose of the bow shock. The spacecraft trajectory is approximately along $-x$ in GSE. The shock normal **n** based on the shock model by Merka *et al.* [26] is [0.993, 0.116, −0.028] in GSE. The upstream Alfvén Mach number (M_A) is ∼7.8. The angle (θ_{Bn}) between the upstream **B** and **n** is about 115°. Other parameters of the shock are the ion beta $\beta_i \sim 1.1$ (based on the OMNI ion temperature and density as the MMS ion instrument was not designed to monitor the solar wind), the electron beta $\beta_e \sim 0.3$, the upstream ion inertial length $d_i \sim 94$ km, the upstream ion gyroperiod ∼6 s, and the magnetosonic Mach number ∼4.

The MMS data employed are from the burst-mode Fast Plasma Investigation [27], the Fluxgate Magnetometer [28], the Search-Coil Magnetometer [29], and the electric field spin-plane [30] and axial [31] double probes in the FIELDS suites [32]. All displayed data are from MMS4. The axial (∼$\hat{z}$GSE) electric-field calibration assumes $E \cdot B = 0$ in 1 s intervals, implying that the dc component of the electric field parallel to **B** for the time scale larger than 1 s is filtered out. The electron velocity distributions are displayed in $v_{\parallel}$-$v_{\perp 1}$ (sliced at the bulk $v_{\perp 2}$) with the phase-space density averaged over a range of $v_{\perp 2}$ and the parallel direction defined by $\hat{b}$ while the two perpendicular directions by $\vec{v}_{\perp 1} = (\hat{b} \times \hat{V}) \times \hat{b}$ and $\vec{v}_{\perp 2} = \hat{b} \times \hat{V}$, where $\hat{b}$ and $\hat{V}$ are the unit vectors of the magnetic field **B** and the electron velocity moment $\mathbf{V}_e$, respectively. The zero parallel velocities in both the spacecraft and the de Hoffmann–Teller (dHT) [33] frames are marked in the distributions as vertical dotted and dashed lines, respectively. The dHT velocity is determined by $V_{\mathrm{HT}} = n \times (V_{i0} \times B_0)/B_n$, where V_{i0} is the upstream ion bulk velocity in the shock frame, $\mathbf{B}_0$ is the upstream magnetic field, and B_n is the normal component of $\mathbf{B}_0$ [34].

Observations.—An overview of the observed shock is presented in Fig. 1. The plasma density compresses from 6 cm^{-3} upstream to 50 cm^{-3} at the ramp [Fig. 1(a)],

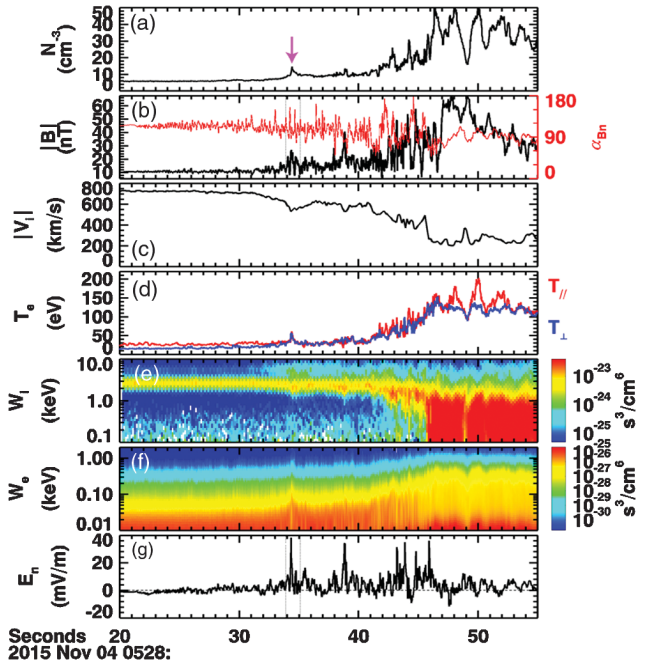

FIG. 1. Overview of Earth's bow shock encountered by the MMS4 spacecraft. (a) The density N. (b) The magnetic field $|\mathbf{B}|$ and the angle between the instantaneous **B** and the shock normal **n**. (c) The bulk ion velocity $|\mathbf{V}_i|$. (d) The electron temperature parallel ($T_{\parallel}$) and perpendicular ($T_{\perp}$) to **B**. The ion (e) and electron (f) phase space density as a function of energy (W) and time. (g) The electric field component along **n** (E_n), averaged to the same cadence as the electron measurements. The magenta arrow marks the time to be zoomed in.

magnetic field magnitude increases from 11 nT upstream to 66 nT [Fig. 1(b)], and the solar wind bulk ion flow decreases from 720 km/s (∼3 keV) to 200 km/s after the ramp [Fig. 1(c)]. The upstream solar wind speed is significantly higher than the usual 400 km/s, enabling the shock to achieve an electron thermal energy gain of approximately 140 eV [Fig. 1(d)], compared to the typical values of a few tens of eV (see Ref. [35] for a relation between the electron thermal energy gain and the upstream solar wind speed and Ref. [11] for the energy budget to heat electrons). Magnetic fluctuations are large both in magnitude and direction (the angle α_{B_n} between **n** and the instantaneous **B** is shown). The ion and electron phase-space densities as functions of energy and time show that the solar wind ion energy decrease [Fig. 1(e)] and electron energization [Fig. 1(f)] take place at discrete locations (e.g., at 052834 and 052839 UT). At these locations, the electric field component along **n** [Fig. 1(g)], the plasma density N, and magnetic field **B** all exhibit sharp enhancements with substantial nonuniformity on the scale of spacecraft separations (approximately 0.2 d_i). The normal component of the electric field (E_n) is thought to be responsible for slowing down the supersonic ion flow and reflecting part of the incoming ions [36]. The first E_n spike [time marked by the magenta arrow in Fig. 1(a)] appears near the time

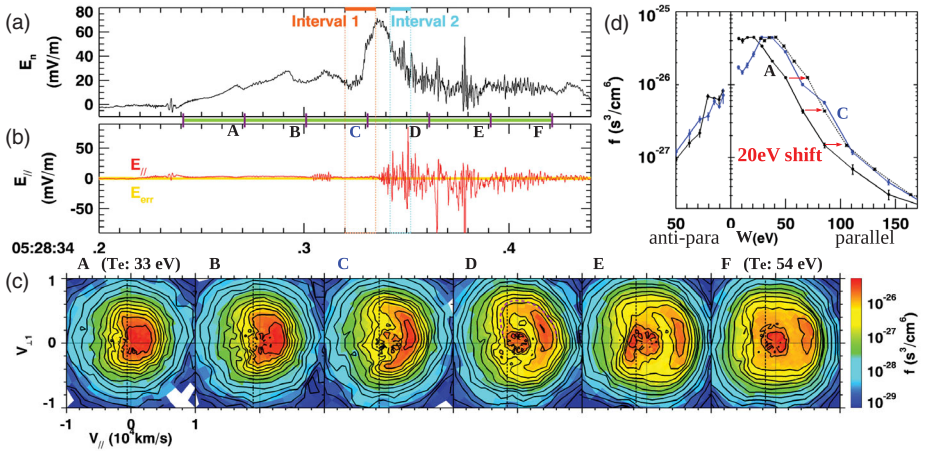

FIG. 2. Electron distributions revealing acceleration and nonlinear relaxation leading to heating. (a)–(b) High-time-resolution data (8192 sample/s) of the first E_n spike (time marked by the magenta arrow in Fig. 1) and the concurrent ac parallel electric field. (c) Sequence of electron distributions in $v_\parallel$-$v_{\perp 1}$. The dHT velocity projected onto the local **B** is marked on each distribution by a vertical dashed line. (d) 1D cuts (taken at the bulk $v_{\perp 1}$ along $v_\parallel$) of distributions A and C shown in energy space.

when the reflected ions are first observed [the population above 3–4 keV at around 052834 UT in Fig. 1(e)].

Figure 2 demonstrates the bulk acceleration and thermalization of the incident solar wind electrons during the first E_n spike [high-resolution measurements are displayed in Fig. 2(a)]. The sequence $A-F$ of electron distributions [Fig. 2(c)] in $v_\parallel - v_{\perp 1}$ shows that (i) solar wind electrons are accelerated along **B** toward the shock (distributions $A-C$); (ii) in distribution C, the acceleration results in a high parallel speed of the electron population peak, leading to a relative drift with respect to the bulk ion parallel speed (~200 km/s) at ~2900 km/s, larger than the electron parallel thermal speed of ~1600 km/s (estimated by $\sqrt{2T/m_e}$ based on a Maxwellian temperature fit to the 1D cut of the distribution along **B**), a condition with high parallel current density and potentially subject to the Buneman instability [37]; (iii) transport of the phase-space density from parallel to antiparallel along an arc (flanked by a purple dashed curve in distribution D), suggesting electron trapping by fast growing waves [38–40]; (iv) counterstreaming populations with unequal $|v_\parallel|$ in both the dHT and spacecraft frames are formed (distribution E), similar to those predicted by a shock microinstability simulation [41]; (v) a thermalized distribution (F) contains a beam as a remnant of the accelerated solar wind electrons, analogous to the beam on a 1D flat-topped distribution observed [6] and modeled [42] previously. The electron temperature T_e (defined as one-third of the trace of the electron pressure tensor divided by the density) increases from 33 eV for distribution A to 54 eV for distribution F. Note that all the reported features are at velocities above the instrument cutoff velocity (after subtracting the spacecraft potential for the photoelectron correction) of 1600 km/s, corresponding to the lowest energy of 7.2 eV in Fig. 2(d). On the other hand, the low-velocity population centered at the origin in distributions D-F and H-L may be due to instrumental effects.

The inflation from distributions A to C occurs only for the part of the phase space with $v_\parallel > 0$. Comparing the 1D cuts of the distributions in the energy space shows a 20 eV energy shift (in the spacecraft frame; a 45 eV shift in the dHT frame) in the direction parallel to **B** [Fig. 2(d)]. No corresponding energy shift in the antiparallel direction is observed.

The bulk acceleration of the incident solar wind electrons moving along **B** and reaching a velocity larger than its parallel thermal spread is directly measured for the first time at the bow shock. The spreading in pitch angle in distribution C creates a partial spherical shell (based on examining slices of the entire distribution) spanning the positive $v_\parallel$ part of the 3D distribution. The 3D structure may need to be taken into account for proper instability considerations. Electrostatic waves linearly polarized along **B** with a plasma-frame phase speed approximately 155 km/s near the expected value for the Buneman wave (~100 km/s based on a 1D theory [37]) are observed at 052834.304-.314 UT [Fig. 2(b)], but the wave amplitude does not grow appreciably, suggesting that the Buneman instability, possibly triggered, is quickly taken over by other processes.

Thermalization in the form of dissipating the parallel electron flow (with respect to ions) into thermal energy is achieved within 90 ms (<30 electron cyclotron periods using the upstream $|B|$), as revealed in distributions $D-F$. Electron transport in the phase space from $v_\parallel > 0$ to $v_\parallel < 0$ occurs in distribution D as shown by the arc extending through $v_{\perp 1} > 0$. The asymmetry with respect to $v_{\perp 1} = 0$ indicates nongyrotropy and possible demagnetization of electrons. The beam in distribution F suggests that the nonlinear current-driven ion acoustic or Buneman instability could be responsible for relaxing the unstable distribution. In 1D, both instabilities are known to spread the original

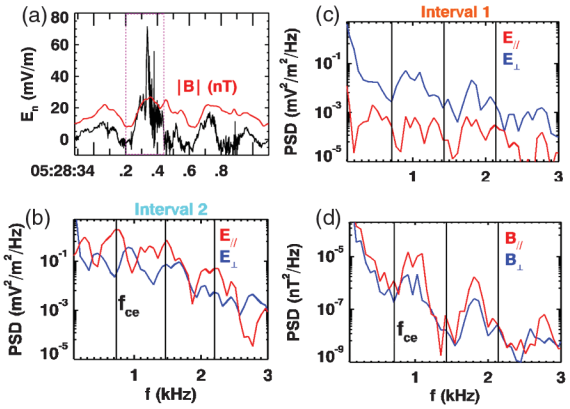

FIG. 3. Analysis of the electric and magnetic fields from the acceleration and relaxation phase to shed light on participating waves and instabilities. (a) Profiles of E_n and $|\mathbf{B}|$ showing that the first E_n spike (in the magenta box) is embedded in an electromagnetic whistler-mode wave. The power spectral densities for the intervals marked blue [interval 2, marked in Figs. 2(a)–2(b)] and orange (interval 1) are presented in (b) and (c)–(d), respectively.

electron stream in the velocity space leaving a remnant beam of the original population in the thermalized distribution [38–39], analogous to the beam in distribution F.

The electric field spike [shown in Fig. 2(a)] associated with the electron acceleration discussed above consists of a sharp central peak embedded in an electromagnetic whistler-mode wave [Fig. 3(a)]. The wave exhibits properties consistent with whistler-mode precursors near collisionless shock ramps [43–44], including right-hand polarization (based on **B** and **E** excluding the central peak, not shown), a frequency higher than the ion cyclotron and lower than the lower hybrid frequencies, a wavelength approximately 30 electron skin depths, and a propagation velocity (based on multispacecraft timing analysis) toward upstream approximately along **n**. Note that the sharp central peak of the E_n spike [>20 mV/m, see Fig. 3(a)] does not have a corresponding magnetic component.

Electric-field fluctuations grow drastically in amplitude [Figs. 2(a)–2(b)] as the phase-space-density transport occurs. The power spectral density (PSD) exhibits enhancements in $E_\parallel$ at multiple electron-cyclotron-frequency ($f_{ce} \sim 733$ Hz) harmonics [Fig. 3(b); the time interval is color coded in blue and marked as interval 2 in Figs. 2(a)–2(b)], indicating the presence of the Bernstein mode [45]. The PSD in $E_\parallel$ is much stronger than that in $E_\perp$ at the f_{ce} harmonics, a feature observed before at interplanetary shocks and interpreted as the ion acoustic waves coupled with the Bernstein mode [20]. These large-amplitude fluctuations exhibit features consistent with the nonlinear ion acoustic waves: (i) broadband waves mainly in $E_\parallel$, (ii) the phase speed (~500 km/s in the plasma frame) comparable to the ion sound speed (~600 km/s), and (3) the plasma-frame frequency (435 Hz) less than the ion plasma frequency (674 Hz) for the near f_{ce} waves.

Electromagnetic electron Bernstein waves are observed during a brief interval [interval 1, color coded in orange and marked in Figs. 2(a)–2(b)] covering the transition between distributions C and D. The PSD in both **E** [Fig. 3(c)] and **B** [Fig. 3(d)] exhibit peaks between the f_{ce} harmonics. The peaks are most pronounced in $E_\perp$ and $B_\parallel$, consistent with that predicted for the electron cyclotron drift instability extended for propagations quasiperpendicular to **B** [45].

Electron distributions in various phases of the acceleration and relaxation are observed throughout the shock. Sample distributions from the main electron temperature ramp (052840-47 UT) along with burst-mode measurements of the electric field, parallel and perpendicular to **B**, are presented in Fig. 4 to provide a glimpse into the

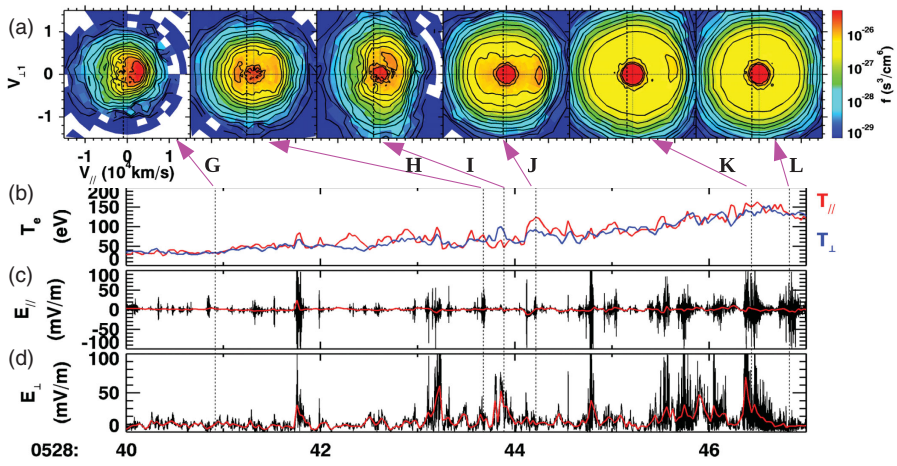

FIG. 4. Sample electron distributions (a) from the main electron temperature (b) ramp (052840-47 UT) along with burst-mode measurements of the electric field parallel (c) and perpendicular (d) to B. Note that the employed velocity range in distributions $G-L$ is 50% larger than that in Fig. 2(c). The burst field data averaged to the electron measurement cadence are presented in red (c)–(d).

cross-shock electron heating. Thermalized distributions with a remnant beam at $v_{\parallel} > 0$ are observed in about half of the total 233 distributions in the shown interval, indicating that electrons are continually being accelerated and thermalized in the T_e ramp. Distribution G [Fig. 4(a)], resembling distribution B, presents the accelerated solar wind electrons as a population shifted in $v_{\parallel} > 0$. A pronounced beam at $v_{\parallel} < 0$, similar to that in distribution E, is present in distribution H with simultaneous enhancements in $E_{\parallel}$ [Fig. 4(c)]. Distribution I with $T_{\perp} > T_{\parallel}$ [Fig. 4(b)] is among a series of nongyrotropic distributions observed concurrently with strong $E_{\perp}$ [Fig. 4(d)]. Distributions J and K are thermalized with remnant beams. The hundreds of electron distributions provide continuous monitoring of the electron phase space in the shock transition layer, showing a heating process that is highly nonadiabatic, far beyond the simple picture of a quasistatic cross-shock potential.

Throughout the shock front, the electron distributions are predominantly anisotropic, despite an on-average equal partition between $T_{\parallel}$ and $T_{\perp}$. Localized variations in $T_{\parallel}$ and $T_{\perp}$ [Fig. 4(b)] often exist with large-amplitude electric-field fluctuations, supporting local anisotropic heating correlated with the strong short-scale electric fields, rather than isotropic heating as suggested in earlier work [19]. Only near the end of the T_e ramp, the distribution functions are more isotropic and the beam is less pronounced (distribution K) or wiped out (distribution L), indicating participation of additional isotropization processes. Detailed analysis of the field fluctuations and their potential role in heating and/or isotropizing electrons is left for future work.

In summary, the measurements reported in this Letter reveal the bulk acceleration of the solar wind electrons and the nonlinear relaxation resulting in heating at a quasiperpendicular shock front. The acceleration is achieved by an electric field embedded in a low-frequency whistler-mode wave, and leads to a high parallel current density. The dominant instability responsible for dissipating the current is likely the nonlinear ion acoustic-Bernstein mode, although the exact signature of the instability in three dimensions is yet to be investigated. Electron distributions resembling the shown examples are observed in other quasiperpendicular shock events with similar Mach numbers and different θ_{B_n} (~60°–82°) configurations. However, the electron heating physics may be quite different for perpendicular shocks. Studies simulating the perpendicular geometry predict electron heating to be due to scattering by the high-frequency electron whistlers [46–47].

Our study raised questions regarding the nature of the cross-shock potential. A collection of the localized strong electric fields (the E_n spikes) may constitute part of the "cross-shock potential." Efforts integrating space observations, simulations, and laboratory experiments with sufficiently high Mach numbers [48] will be highly valuable to address the true nature of the cross-shock potential and the associated electron heating.

The authors thank the entire MMS team for developing and operating the mission. The research was supported in part by DOE Grant No. DESC0016278, NSF Grants No. AGS-1202537, No. AGS-1543598, and No. AGS-1552142, and by the NASA MMS project. The French involvement (SCM) on MMS is supported by CNES and CNRS. The data are available at the MMS Science Data Center.

*lijen@mailaps.org

[1] P. Ghavamian, S. J. Schwartz, J. Mitchell, A. Masters, and J. M. Laming, Space Sci. Rev. **178**, 633 (2013).
[2] V. Krasnoselskikh *et al.*, Space Sci. Rev. **178**, 535 (2013).
[3] A. Bamba, R. Yamazaki, M. Ueno, and K. Koyama, Astrophys. J. **589**, 827 (2003).
[4] M. E. Dieckmann, A. Bret, G. Sarri, E. Perez Alvaro, I. Kourakis, and M. Borghesi, Plasma Phys. Controlled Fusion **54**, 085015 (2012).
[5] N. Sckopke, G. Paschmann, S. J. Bame, J. T. Gosling, and C. T. Russell, J. Geophys. Res. **88**, 6121 (1983).
[6] W. C. Feldman, R. C. Anderson, S. J. Bame, S. P. Gary, J. T. Gosling, D. J. McComas, M. F. Thomsen, G. Paschmann, and M. M. Hoppe, J. Geophys. Res. **88**, 96 (1983).
[7] J. D. Scudder, A. Mangeney, C. Lacombe, C. C. Harvey, and T. L. Aggson, J. Geophys. Res. **91**, 11053 (1986).
[8] J. D. Scudder, Adv. Space Res. **15**, 181 (1995).
[9] A. J. Hull, J. D. Scudder, D. E. Larson, and R. Lin, J. Geophys. Res. **106**, 15711 (2001).
[10] B. Lefebvre, S. J. Schwartz, A. F. Fazakerley, and P. Décréau, J. Geophys. Res. **112** (2007).
[11] S. J. Schwartz, J. Geophys. Res. **93**, 12923 (1988).
[12] S. J. Schwartz, J. Geophys. Res. **119**, 1507 (2014).
[13] S. J. Schwartz, E. Henley, J. Mitchell, and V. Krasnoselskikh, Phys. Rev. Lett. **107**, 215002 (2011).
[14] M. D. Montgomery, J. R. Asbridge, and S. J. Bame, J. Geophys. Res. **75**, 1217 (1970).
[15] S. D. Bale, P. J. Kellogg, D. E. Larsen, R. P. Lin, K. Goetz, and R. P. Lepping, Geophys. Res. Lett. **25**, 2929 (1998).
[16] S. D. Bale and F. S. Mozer, Phys. Rev. Lett. **98**, 205001 (2007).
[17] A. J. Hull, D. E. Larson, M. Wilber, J. D. Scudder, F. S. Mozer, C. T. Russell, and S. D. Bale, Geophys. Res. Lett. **33**, L15104 (2006).
[18] V. See, R. F. Cameron, and S. J. Schwartz, Ann. Geophys. **31**, 639 (2013).
[19] F. S. Mozer and D. Sundkvist, J. Geophys. Res. **118**, 5415 (2013).
[20] L. B. Wilson III, C. A. Cattell, P. J. Kellogg, K. Goetz, K. Kersten, J. C. Kasper, A. Szabo, and M. Wilber, J. Geophys. Res. **115**, A12104 (2010).
[21] L. B. Wilson, D. G. Sibeck, A. W. Breneman, O. Le Contel, C. Cully, D. L. Turner, V. Angelopoulos, and D. M. Malaspina, J. Geophys. Res. **119**, 6475 (2014).
[22] M. Balikhin, M. Gedalin, and A. Petrukovich, Phys. Rev. Lett. **70**, 1259 (1993).

[23] B. Lembège *et al.*, J. Geophys. Res. **108**, 1256 (2003).
[24] M. Balikhin, V. V. Krasnosel'skikh, L. J. C. Woolliscroft, and M. Gedalin, J. Geophys. Res. **103**, 2029 (1998).
[25] J. L. Burch *et al.*, Science **352**, aaf2939 (2016).
[26] J. Merka, A. Szabo, J. A. Slavin, and M. Peredo, J. Geophys. Res. **110**, A04202 (2005).
[27] C. Pollock *et al.*, Space Sci. Rev. **199**, 331 (2016).
[28] C. T. Russell *et al.*, Space Sci. Rev. **199**, 189 (2016).
[29] O. Le Contel *et al.*, Space Sci. Rev. **199**, 257 (2016).
[30] P.-A. Lindqvist *et al.*, Space Sci. Rev. **199**, 137 (2016).
[31] R. E. Ergun *et al.*, Space Sci. Rev. **199**, 167 (2016).
[32] R. B. Torbert *et al.*, Space Sci. Rev. **199**, 105 (2016).
[33] F. de Hoffmann and E. Teller, Phys. Rev. **80**, 692 (1950).
[34] S. J. Schwartz, ISSI Sci. Rep. Ser. **SR-001**, 249 (1998).
[35] M. F. Thomsen, M. M. Mellott, J. A. Stansberry, S. J. Bame, J. T. Gosling, and C. T. Russell, J. Geophys. Res. **92**, 10119 (1987).
[36] C. C. Goodrich and J. D. Scudder, J. Geophys. Res. **89**, 6654 (1984).
[37] O. Buneman, Phys. Rev. Lett. **1**, 8 (1958).
[38] Y. Omura, W. J. Heikkila, T. Umeda, K. Ninomiya, and H. Matsumoto, J. Geophys. Res. **108**, 1197 (2003).
[39] Y. Omura, H. Matsumoto, T. Miyake, and H. Kojima, J. Geophys. Res. **101**, 2685 (1996).
[40] S. Matsukiyo and M. Scholer, J. Geophys. Res. **117** (2012).
[41] S. Matsukiyo and M. Scholer, J. Geophys. Res. **111**, A06104 (2006).
[42] M. F. Thomsen, H. C. Barr, S. Peter Gary, W. C. Feldman, and T. E. Cole, J. Geophys. Res. **88**, 3035 (1983).
[43] L. B. Wilson, III, A. Koval, A. Szabo, M. L. Stevens, J. C. Kasper, C. A. Cattell, and V. V. Krasnoselskikh, J. Geophys. Res. **122**, 9115 (2017).
[44] M. Scholer and D. Burgess, Phys. Plasmas **14**, 072103 (2007).
[45] L. Muschietti and B. Lembège, Ann. Geophys. **35**, 1093 (2017).
[46] X. Guo, L. Sironi, and R. Narayan, Astro. Phys. J. **851**, 134 (2017).
[47] X. Guo, L. Sironi, and R. Narayan, arXiv:1712.03239.
[48] D. Schaeffer, W. Fox, D. Haberberger, G. Fiksel, A. Bhattacharjee, D. H. Barnak, S. X. Hu, and K. Germaschewski, Phys. Rev. Lett. **119**, 025001 (2017).